



Crystallization, cyanamide defect and ion induction of carbon nitride: Exciton polarization dissociation, charge transfer and surface electron density for enhanced hydrogen evolution

Jili Yuan^a, Yanhong Tang^{a,*}, Xuanying Yi^b, Chengbin Liu^{b,*}, Can Li^{c,*}, Yunxiong Zeng^b, Shenglian Luo^b

^a College of Materials Science and Engineering, Hunan University, Changsha, 410082, PR China

^b State Key Laboratory of Chemo/Biosensing and Chemometrics, Hunan University, Changsha, 410082, PR China

^c College of Materials Science and Engineering, China Jiliang University, Hangzhou, 310018, PR China

ARTICLE INFO

Keywords:

Carbon nitride
Exciton polarization dissociation
Charge transfer
Surface electron density
Hydrogen evolution

ABSTRACT

Exciton polarization dissociation, charge transfer and surface electron density in photocatalysts are crucial for photocatalytic hydrogen evolution reactions (HERs). In this study, crystalline carbon nitride with cyanamide defect edges (crystalline CCN) was synthesized by one step polymerization of urea in the presence of KCl. The texture and electronic band structure of carbon nitrides could be facily tailored by changing KCl dosage. The light absorption edge of crystalline CCN extended to 736 nm due to $n \rightarrow \pi^*$ electron transition. The enhanced dielectric constants of crystalline carbon nitrides promoted exciton polarization dissociation. The small effective electron mass (m_e^*) in crystalline CCN facilitated m_e^* diffusion. The efficient separation of electrons and holes benefited the formation of internal electric field, showing an 8.56-fold promotion in electron transfer compared to pristine CN. Significantly, femtosecond time-resolved transient absorption demonstrated that the surface electron density on crystalline CCN was enhanced in the presence of salt ions (NaCl). As a result, crystalline CCN exhibited 14.9 times higher HER rate than pristine CN under visible light irradiation. The apparent quantum yield for H_2 evolution on crystalline CCN reached to 42% at 420 nm and 9% at 500 nm. This study gets a comprehensive understanding of photocatalytic HERs using carbon nitride photocatalysts.

1. Introduction

Photocatalytic hydrogen production is an attractive strategy for the conversion of solar energy into hydrogen energy [1]. Polymeric carbon nitride (CN) based photocatalysts have received much attention due to their visible-light response, cost-effective synthesis and high stability [2]. However, the low solar-to-hydrogen efficiency limits their practical applications [3]. Polymeric CN has a short-range organic semiconductor lattice and the charges are easily localized in space, which makes CN bear sluggish exciton binding energy (E_b), resulting in a low exciton dissociation and poor charge transfer [4,5].

The electron transport in CNs is perpendicular to the melon planar direction, so the layer stacking has an important effect on interlayer exciton dissociation and charge transfer [6,7]. Small stacking distance contributes to intense polarization or charge transfer between layers. Partial positive and negative charges on neighboring layers and high conjugation can make tight stacking, promoting free charge carrier

generation and transport within the stacks. The stacking can be regulated by defect engineering [8], morphology control [9–11], and crystallization [12,13]. In addition, in-plane separation and transport of excitons is key to generate enough free charge carriers for photocatalytic hydrogen evolution reactions (HERs). The in-plane potential difference between edges and interior states or junction interface benefits free charge carrier generation [14–17]. For example, cyanamide edges or donor-acceptor structures in melon-based framework benefit the generation and mobility of free charge carriers [18–24]. However, the relationship between CN structure and exciton polarization dissociation (or charge transfer) lacks systematic study.

In this study, crystalline cyanamide carbon nitride (crystalline CCN) was synthesized by one step polymerization of urea in the presence of KCl. The texture and electronic band structure of polymeric carbon nitrides could be tailored by changing KCl dosage. Density-functional theory (DFT) calculations were performed to gain an insight into the relationship between the polymer structures and the bandgaps. The

* Corresponding authors.

E-mail addresses: tangyh@hnu.edu.cn (Y. Tang), chem_cbliu@hnu.edu.cn (C. Liu), canli1983@gmail.com (C. Li).

<https://doi.org/10.1016/j.apcatb.2019.03.069>

Received 5 September 2018; Received in revised form 15 January 2019; Accepted 27 March 2019

Available online 27 March 2019

0926-3373/ © 2019 Elsevier B.V. All rights reserved.

effects of dielectric properties, exciton dissociation and charge transfer on HERs were systemically studied.

2. Experimental

2.1. Chemical materials

Nafion solution (5 wt%), NaSO₄, K₂SO₄, KBr, KCl, NaCl, BaCl₂, triethanolamine (TEOA), urea and H₂PtCl₆·6H₂O were obtained from Sinopharm Chemical Reagent Co. Ltd and used without further purification. Ultrapure (Milli-Q) water was used to prepare all solutions for photocatalytic hydrogen reactions.

2.2. Synthesis of CN and CCN

Typically, 10 g of urea was dissolved in deionized water, the resulting solution was heated at 80 °C for 30 min, and the solution was frozen at -80 °C for 24 h followed by freeze drying. The solids were placed into a sealed crucible and heated at 600 °C for 2 h to get CN (amorphous).

Preparation of crystalline CN, CCN (amorphous) and crystalline CCN: 10 g of urea was dissolved in a KCl aqueous solution (0.03, 0.30 and 3.00 g KCl in 10 mL H₂O, respectively). The resulting solution was heated at 80 °C for 30 min, and then was frozen at -80 °C for 24 h followed by freeze drying. The solid was further calcined in a tube furnace at 600 °C for 2 h. After cooling them to the room temperature, the collected solids were washed three times with deionized water and dried in vacuum for overnight. The products were labelled by crystalline CN, CCN and crystalline CCN using 0.03, 0.30 and 3.00 g KCl during urea polymerization, respectively.

2.3. Characterizations

The powder X-ray diffraction (XRD) patterns were collected on a Bruker DAVINCI D8 ADVANCE diffractometer equipped with a Cu-Kα source. The morphologies of the samples were examined by a transmission electron microscope (TEM) (JEOL, JEM-2100 F) and a scanning electron microscope (SEM) (FEI XL-30E) at an accelerating voltage of 10 kV. Electron energy loss spectra (EELS) were from TEM equipped with a Gatan GIF Quantum. The Fourier transform infrared (FTIR) spectra were recorded on a Perkin Elmer GX spectrophotometer over the range of 4000–400 cm⁻¹. The C, N and O contents were measured by a Vario EL III elemental analyzer. The chemical element compositions were analyzed by an energy disperse spectroscopy (EDS) (Tecnai G2 F20 S-TWIN). Solid-state nuclear magnetic resonance (NMR) spectra of ¹³C and ¹⁵N were recorded on a Bruker AVANCE III 400 MHz WB solid-state NMR spectrometer at room temperature. UV–vis diffuse reflectance spectra (DRS) were measured using a Cary 5000 spectrophotometer fitted with an integrating sphere from 200 to 800 nm with BaSO₄ as the reference. X-ray photoelectron spectra (XPS) were recorded on a Quantum 2000 Scanning ESCA Microprobe (Physical Electronics) using monochromatic Al Kα radiation (1486.7 eV) as the X-ray source. Dielectric constant was determined by a Vector network analyzer (VNA) (PNA-N5244 A). The specific surface area was determined by the Brunauer-Emmett-Teller (BET) method with N₂ adsorption at 77 K (BELSORP-mini II). The photoluminescence (PL) at 298 K and transient PL at 77 K were monitored at a Perkin Elmer Luminescence Spectrometer (LS 50 B) with an excitation wavelength of 330 nm.

2.4. Photoelectrochemical measurements

The photoelectrochemical properties were investigated in a 0.5 M Na₂SO₄ aqueous solution using a CHI electrochemical analyzer (USA) equipped with a three-electrode system. The catalyst-coated FTO glass, a Pt foil and an Ag/AgCl electrode were used as the working electrode,

the counter-electrode and the reference electrode, respectively. A 300 W Xe arc lamp equipped with a 420 nm cutoff filter was utilized as the light source. The electrochemical impedance spectra (EIS) were recorded at 1.0 V vs Ag/AgCl over a frequency range of 1 MHz to 0.01 Hz. The photocurrent with ON/OFF cycles was measured at 0 V vs Ag/AgCl. Mott–Schottky plots were obtained under direct current potential polarization at different frequencies (1000, 1500 and 2000 Hz). The potential ranged from -0.4 to 1.6 V (vs Ag/AgCl). For the fabrication of working electrode, an FTO glass was sequentially cleaned by ultrasonication in deionized water, absolute ethanol and isopropanol for 15 min, and then dried in vacuum. 5 mg of photocatalysts and 10 μL of Nafion solution (5 wt%) were dispersed in 1 mL of water/isopropanol solvent (3:1 v/v) under sonication to get a homogeneous colloid. Then, 110 μL of the colloid was deposited onto the cleaned FTO glass. The catalyst-coated FTO was dried in air to get the working electrode. The catalyst on the FTO electrode was 1.67 mg cm⁻² (active area of 3 cm²).

2.5. Photocatalytic activity measurements

The photocatalytic HERs were carried out in a Pyrex glass reaction cell containing 80 mL 15 vol% of TEOA aqueous solution. 50 mg of photocatalysts were used. 3 wt% Pt co-catalyst was *in situ* photo-deposited on the surface of the photocatalysts. Before irradiation, the air in the reaction cell was removed by bubbling N₂. A 300 W Xenon lamp (Perfect light, China) with a 420 nm cut-off filter was used as the visible-light source. The lamp was positioned 10 cm away from the reactor where the focused intensity on the cell was 120 mW·cm⁻². The H₂ was analyzed by a gas chromatography (Shimadzu, GC2010) combined with 5 Å molecular sieve column (Plot Q column, 0.32 μm) and high purity argon as carrier gas (99.999%).

2.6. Quantum efficiency calculations

The apparent quantum yield (AQY) for H₂ evolution was measured under monochromatic light irradiation (420 and 500 nm) using a 300 W Xe lamp with specific band-pass filters. The irradiation area was 5.94 cm² and the average irradiation intensity was 2.55 mW·cm⁻². Depending on the amount of H₂ produced in one hour, the AQY was calculated as follows:

$$\text{AQY} = \frac{\text{Number of reacted electrons}}{\text{Number of incident photons}} \times 100\% \quad (1)$$

$$\frac{\text{Number of evolved hydrogen molecules} \times 2}{\text{Number of incident photons}} \times 100\% \quad (2)$$

$$\text{Number of evolved H}_2 \text{ molecules} = 2 \times M \times N_A \quad (3)$$

$$\text{Number of incident photons} = \frac{E\lambda}{hc} \quad (4)$$

Where, M is the mole number of H₂ molecules (mol), N_A is Avogadro constant (6.022 × 10²³/mol), h is Plank constant (6.626 × 10⁻³⁴ J s), c is the speed of light (3 × 10⁸ m/s), and λ is the monochromatic light wavelength (m).

2.7. Computational methods

The first principles calculations in the framework of density functional theory (DFT), including structural, electronic and optical performances, were carried out based on the Cambridge Sequential Total Energy Package known as CASTEP [25]. The exchange–correlation interactions were treated by generalized gradient approximation with norm-conserving pseudopotentials parameterized by Perdew, Burke and Ernzerhof. An energy cutoff of 550 eV was used. The k-point sampling sets of 5 × 5 × 4, 5 × 5 × 4, 2 × 3 × 10 and 3 × 3 × 4 were tested for CN, CCN, crystalline CN and crystalline CCN, respectively. A

force tolerance of $0.01 \text{ eV } \text{\AA}^{-1}$, energy tolerance of $5.0 \times 10^{-7} \text{ eV}$ per atom and maximum displacement of $5.0 \times 10^{-4} \text{ \AA}$ were considered. Each atom in the storage models was allowed to relax to the minimum in the enthalpy without any constraints. The structural optimization and transition states were calculated using DMol3 code [26]. The generalized gradient approximation with the Perdew–Burke–Ernzerhof functional and all-electron double numerical basis set with polarized function were employed [27]. The self-consistent field tolerance of $1.0 \times 10^{-6} \text{ Ha}$ and smearing of 0.005 Ha were set for the calculations of the highest occupied molecular orbital (HOMO) and the lowest unoccupied molecular orbital (LUMO).

2.8. Femtosecond time-resolved transient absorption (fs-TA)

Samples were irradiated with the 365-nm output using a Coherent, Inc./Light Conversion OPerA Solo optical parametric amplifier that was pumped with 50 fs pulses using a 1 kHz Ti: sapphire amplifier (LibraHE, Coherent, Inc.) to generate 0.41×10^{15} – 2.5×10^{15} excitations/ cm^2 /pulse within the sample. Supercontinuum probe pulses ($\sim 200 \text{ fs}$) were generated by focusing a fraction of the 800 nm amplifier output onto CaF_2 or sapphire plates. The spectra were collected with a CMOS sensor and InGaAs fiber-coupled multichannel photodiode array spectrometer and plotted as the differential optical density $\Delta\text{OD} = \log_{10}[I_0 \text{ sample}/I_{\text{ex sample}} \times I_{\text{ex ref}}/I_0 \text{ ref}]$. Samples were irradiated with spatially aligned pump and probe beams, and the probe beam was temporally delayed from the pump using a mechanical delay line (Ultrafast Systems). Kinetics were recorded with random time steps to minimize any influence of sample degradation over the time of the experiment. The estimated absorbed photon flux was not corrected for laser scatter. The spectra were measured in a 2 mm path length quartz cuvette under continuous stirring.

3. Results and discussion

Pristine CN was synthesized by direct condensation of urea. Crystalline CN, CCN and crystalline CCN were synthesized by urea condensation in the presence of different amount of KCl (Scheme S1, Supporting Information). The layer-stacking modes were examined by XRD (Fig. S1a). The amorphous samples (CN and CCN) showed two peaks at 12.7° and 27.6° , ascribed to the (100) in-plane arrangement distance of nitrogen-linked heptazine units and the (002) π - π interlayer stacking, respectively [28]. For crystalline CN and crystalline CCN, the (100) peak shifted to 11.0° , revealing an extended in-plane arrangement distance, and the (002) peak shifted to 28.1° , implying a compacted packing and planarization of undulated heptazine layers [29]. Furthermore, the (100) and (002) peaks became stronger, indicative of an improved crystallinity. Both crystalline CN and crystalline CCN was further confirmed by the high-resolution TEM (HRTEM) images (Fig. 1a–c for crystalline CN, Fig. 1d–f for crystalline CCN). The TEM contrast intensity profiles revealed a spacing of 0.317 nm for the (002) interplanar distance and a fringe separation of 0.96 nm for the (100) in-plane distance (Fig. 1c and f). Moreover, the fast Fourier transform (FFT) patterns clearly presented the diffraction spots (insets, Fig. 1c and f), revealing a good crystallinity in the crystalline samples.

The FTIR spectra are given to determine their chemical structures (Fig. S1b). All the samples showed an out-of-plane bending mode of heptazine rings at 810 cm^{-1} , N–C \equiv N rings in melon framework at 900 – 1800 cm^{-1} , and N–H stretching vibrations at 3000 – 3500 cm^{-1} . Both CCN and crystalline CCN showed two new absorption bands at 1166 cm^{-1} and 2170 cm^{-1} related to the asymmetric vibration of C–N–C bonds in K–NC $_2$ groups and the asymmetric stretching vibration of C \equiv N groups, respectively [30,31]. The peak at 2400 cm^{-1} was C=O asymmetric stretching from the CO_2 in the air. The chemical structures of CCN and crystalline CCN were further determined by ^{13}C and ^{15}N NMR spectra (Fig. S1c–f). Both CCN and crystalline CCN showed $^{13}\text{C}\{^1\text{H}\}$ resonances at 121.1 , 157.1 , 164.8 , 172.9 and

176.4 ppm ascribed to $-\text{C}\equiv\text{N}$, CN_3 , $\text{CN}_2(\text{NH})$, $\text{CN}_2(\text{N}-)$ and $=\text{N}-\text{C}\equiv\text{N}$, respectively [32,33]. Compared with CCN, crystalline CCN showed a stronger CN_3 intensity, meaning the more complete tri-s-triazine rings in crystalline CCN. Moreover, the ^{15}N peak intensity of NC_3 in crystalline CCN was higher than that in CCN, indicative of a higher condensation degree of crystalline CCN.

The element compositions determined by organic elemental analysis method were listed in Table S1. The ratios of C to N for crystalline CN and crystalline CCN increased compared to those for CN and CCN, respectively, due to the hybridization of N–C \equiv N terminals into heptazine units in crystalline samples (Scheme S1). Compared with CN and crystalline CN, CCN and crystalline CCN showed higher molar ratios of O to C, meaning the introduction of oxygen-containing groups. The C, N, K Cl, and O elementals were examined by XPS (Fig. S2 and Table S2). K element was detected only in CCN and crystalline CCN, and Cl elemental was absence in all the samples, indicative of the formation of K–C \equiv N in CCN and crystalline CCN. The C/N molar ratios of 0.726 for crystalline CN and 0.742 for crystalline CCN were closer to the theoretical value of idealized g- C_3N_4 (0.75) than 0.714 for CN and 0.719 for CCN. The results indicated that the hybridization of N–C \equiv N terminals into heptazine units enhanced the crystallization. All samples showed nearly identical XPS peaks of C and N in N–C \equiv N ($\text{N}_{2\text{C}}$) (Fig. 2a and b), indicating that the sp^2 hybridized heptazine units were not destructed after the introduction of N–C \equiv N in CCN. Expectedly, both CCN and crystalline CCN showed the C peak of $-\text{C}\equiv\text{N}$ at 286.4 eV [34]. The peak of N1s at 397.2 eV in CCN and crystalline CCN was attributed to the negatively charged C–N $^-$ –C groups (Fig. 2b) [35]. To further verify the C–N $^-$ –C groups, energy loss near-edge structure (ELNES) spectra were applied to examine the chemical states of C and N atoms. The peaks at 402.3 , 403.0 , 410.3 and 411.1 eV related to the N $1\text{s} \rightarrow \pi^*/\sigma^*$ transitions were observed in CN and crystalline CCN (Fig. 2c). Compared with CN, crystalline CCN showed lower energies of N $1\text{s} \rightarrow \pi^*/\sigma^*$, indicating that the N in crystalline CCN was negatively charged to form C–N $^-$ –C [36]. In contrast, the energy of C $1\text{s} \rightarrow \pi^*$ in crystalline CCN was higher than that of CN (Fig. 2d), indicating a reduced electron cloudy of the C next to negatively charged N. The C–N $^-$ –C groups were neutralized by K^+ . The structural refinement in the molten salt (KCl/KCNO) made a two-dimension layer stacking to one-dimension porous nanobelt structure (crystalline CCN) (Fig. S3 and S4), resulting in a slight increase of specific surface area (Fig. S5 and Tables S3). TEM elemental mapping showed a homogeneous distribution of C, N and K in crystalline CCN and no Cl was detected (Fig. S6).

The optical properties of the samples are shown in Fig. 3a. All the samples showed an absorption peak at approximately 440 nm for the $\pi \rightarrow \pi^*$ electron transition in heptazine rings [37,38]. Compared to CN, the samples (CCN, crystalline CN and crystalline CCN, especially crystalline CCN) showed an absorption redshift. In addition, it is well-known that the organics with unsaturated heteroatomic groups have n electrons and p electrons. Electrons at n orbital can be excited to π^* orbital by the light with a certain frequency, which is called the $n \rightarrow \pi^*$ transition [39]. The new absorption band of 450 – 670 nm in CCN was ascribed to the effective overlap of n orbital and p orbital in cyano groups [40–43]. However, crystalline CCN showed a wider absorption band from 450 to 736 nm , due to not only the effective overlap of n orbital and p orbital in cyano groups, but also well planarized layers (Fig. S7). According to the plots of transformed Kubelka-Munk function vs photon energy, the band gap was reduced from 2.76 eV for CN to 2.31 eV for crystalline CCN and to 2.56 eV for CCN and crystalline CN (Fig. S8). DFT calculations were performed to understand the relationship between structures and bandgaps (Fig. S9 and S10). The trend of bandgap changes was the same as the experimental results. Narrowed bandgap facilitates electron diffusion via polaron hopping mechanism [44]. Based on the valence band (VB) XPS spectra, the VBs were 2.20 , 2.14 , 2.20 and 1.92 eV for CN, crystalline CN, CCN and crystalline CCN, respectively (Fig. S11). The corresponding VBs were 1.64 , 1.58 , 1.64 and 1.34 V vs NHE at pH 7 according to $E_{\text{NHE}}/V = \Phi +$

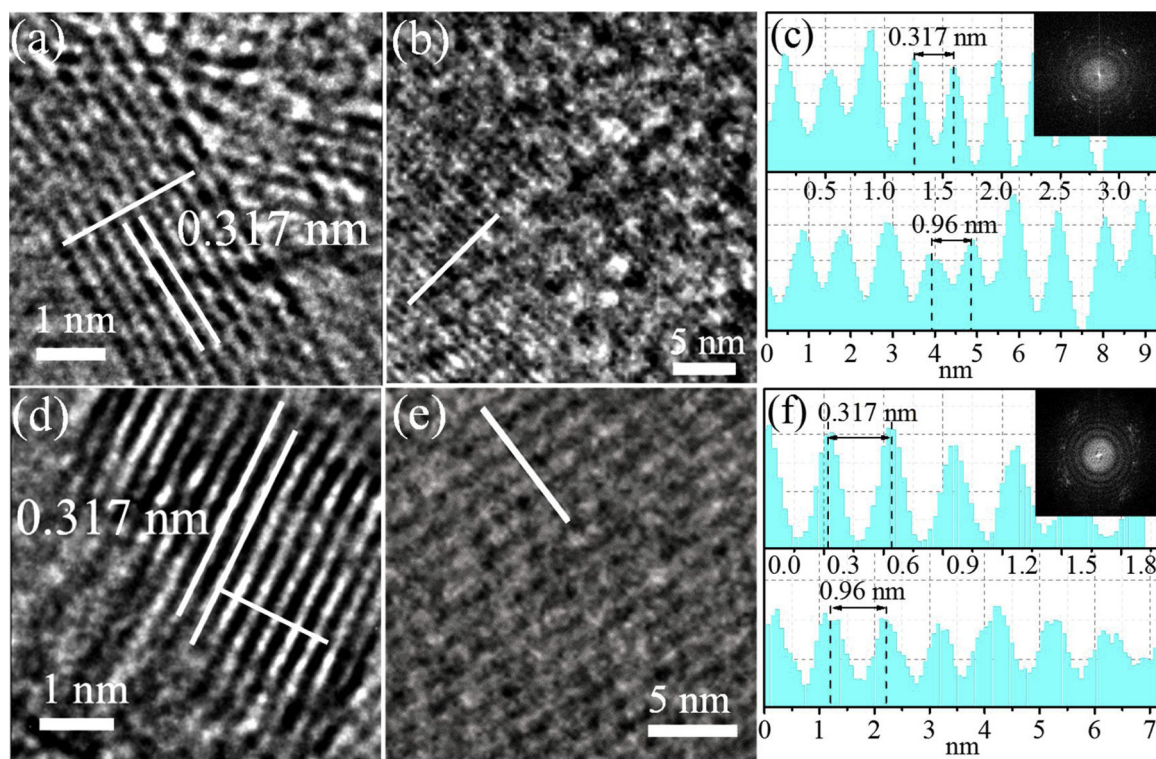


Fig. 1. (a and b) HRTEM images of crystalline CN. (c) TEM contrast intensity profile along the white line in (a) (top) and (b) (down) (inset is FFT pattern). (d and e) HRTEM images of crystalline CCN. (f) TEM contrast intensity profile along the white line in (d) (top) and (e) (down) (inset is FFT pattern).

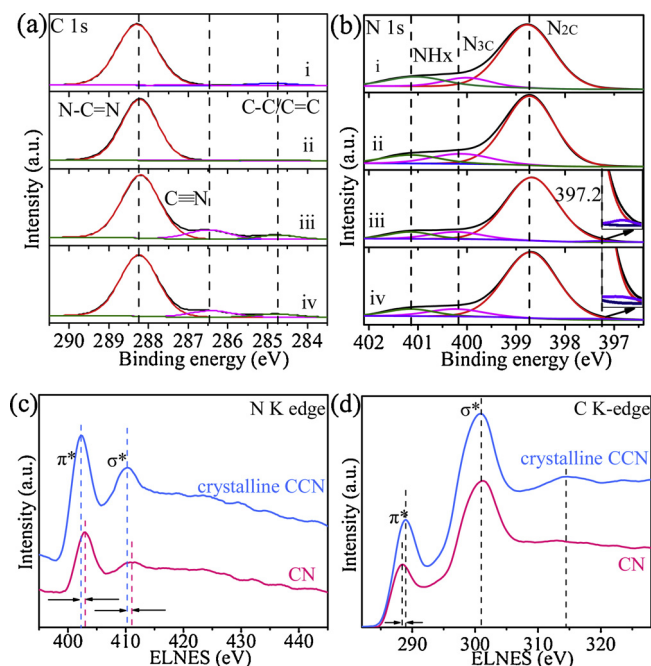


Fig. 2. High resolution XPS spectra of C1s (a) and N1s (b) of (i) CN, (ii) crystalline CN, (iii) CCN and (iv) crystalline CCN. (c) N K-edge and (d) C K-edge ELNES spectra of CN and crystalline CN.

$V_B = -4.44$ (E_{NHE} : potential of normal hydrogen electrode; Φ of 3.88 eV: the electron work function of the analyzer) [45]. The calculated conductive bands (CBs) were -1.12, -0.98, -0.92 and -0.97 V vs NHE for CN, crystalline CN and crystalline CCN, respectively (Fig. 3b). These CBs were consistent with those from Mott-Schottky plots (Fig. S12). These CB levels thermodynamically enable proton reduction for H_2 evolution.

The separation efficiency of photoexcited charge carriers were

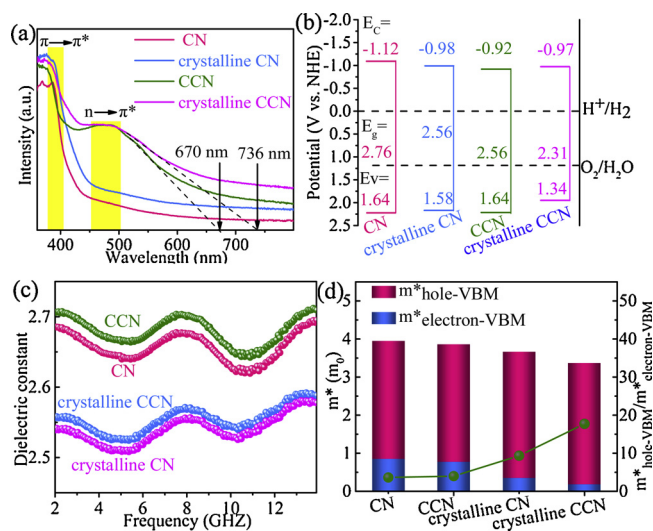


Fig. 3. (a) UV-vis DRS, (b) bandgap alignments, (c) dielectric constant and (d) effective mass approximation for CN, crystalline CN, CCN and crystalline CCN.

investigated by dielectric constant (ϵ_r) and delocalized electrons. As shown in Fig. 3c and Table S4, the lower dielectric constants of crystalline CN and crystalline CCN than CN and CCN indicated that the charges in the crystalline samples could be more easily transferred. In addition, CCN and crystalline CCN showed higher dielectric constants than CN and crystalline CN, respectively, possibly due to the uneven charge distribution in CCN and the charged structure ($C-N^--C$) in crystalline CCN. Higher dielectric constant is in favor of exciton polarization dissociation [46]. Effective mass (m^*) approximation was determined by First-principles calculations to evaluate free charge carrier mobility in semiconductors. Smaller m^* has higher mobility [47]. The predicted m_e^* (electron) in crystalline samples especially crystalline CCN was smaller than that in amorphous samples (Fig. 3d),

which facilitated the diffusion of m_e^* , leaving m_h^* (hole) at VB. Thus, their recombination could be effectively inhibited in crystalline CCN. Efficient separation of electrons and holes benefits the formation of internal electric field, resulting in a polarized surface. The partial density of state (PDOS) calculations for crystalline CN and crystalline CCN showed that both C2p and N2p orbitals contributed to their CBs while only N2p orbitals contributed to their VBs (Fig. S13) [48]. Compared to crystalline CN, crystalline CCN had a sharpened and reinforced C 2p peak, indicative of a more negatively-charged surface from the higher migration of electrons. DFT calculations were performed to evaluate the effect of cyanamide on exciton dissociation in crystalline CCN. The cyanamide edges had lower HOMO (-0.23 eV) and LUMO (1.25 eV) levels compared to the eigen (interior) states (-0.21 for HOMO and 1.33 eV for LUMO) (Fig. S14 a and b). Therefore, the generated electrons would migrate to cyanamide edges while the generated holes would migrate to eigen regions (Fig. S14c and Fig. S15). An electron paramagnetic resonance (EPR) analysis was performed to study the electronic structures in CN, crystalline CN, CCN and crystalline CCN (Fig. S16). A strong EPR signal in single Lorentzian line was observed in all the polymers. The signal originated from the unpaired electrons on sp^2 -carbon atoms of the aromatic rings in π -bonded clusters, which benefited the migration of charge carriers [49]. The strongest peak intensity in crystalline CCN indicated a highly conjugated molecular structure, which promoted the generation of photoinduced charge carriers. The exciton dissociation and charge transfer in crystalline CCN is illustrated as Scheme 1.

Photoluminescence (PL) measurements were performed to investigate the excitonic process. All samples showed an obvious $\pi^* \rightarrow \pi$ emission peak at 450 nm (Fig. 4a), which originated from the radiative decay of singlet excitons in heptazine matrix. Crystalline CCN exhibited the poorest $\pi^* \rightarrow \pi$ emission intensity due to reduced population of singlet excitons. In addition, crystalline CCN showed an obvious $\pi^* \rightarrow n$ emission peak at 570 nm while CCN presented a weak $\pi^* \rightarrow n$ emission peak at 540 ± 10 nm, due to the low planarization degree of CCN [39]. Time-resolved fluorescence (TRF) spectra can reflect the average radiative lifetimes (τ_A) of charge carriers. As shown in Fig. 4b and Table S5, the emission lifetimes of components for crystalline CCN ($\tau_1 = 1.14$ ns, $\tau_2 = 4.51$ ns) and CCN ($\tau_1 = 1.53$ ns, $\tau_2 = 5.56$ ns) were shorter than those for crystalline CN ($\tau_1 = 1.69$ ns, $\tau_2 = 6.79$ ns) and CN ($\tau_1 = 2.09$ ns, $\tau_2 = 8.03$ ns). The shorter lifetime component of τ_1 is originated from the nonradiative quenching, whereas the longer one of τ_2 represents the recombination of free exciton in the materials [50,51]. Based on the fitted fluorescence decay components (Table S5), the calculated τ_A values of CN, crystalline CN, CCN and crystalline CCN were 6.93, 5.15, 4.90 and 3.87 ns, respectively (Fig. 4b). The remarkably quenched emission intensity and the dramatically reduced

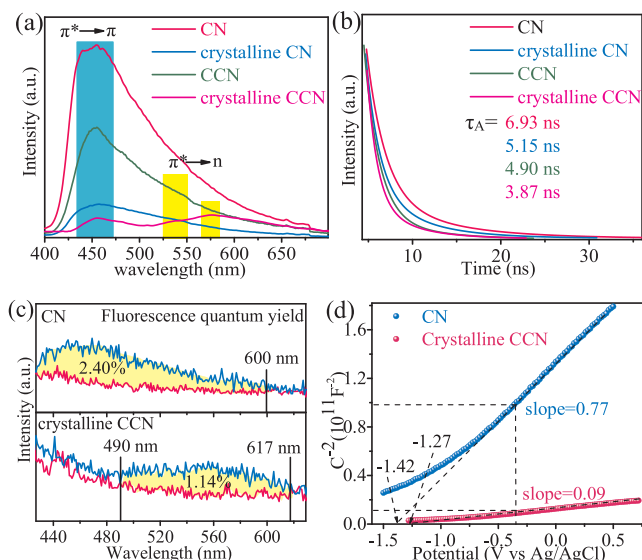


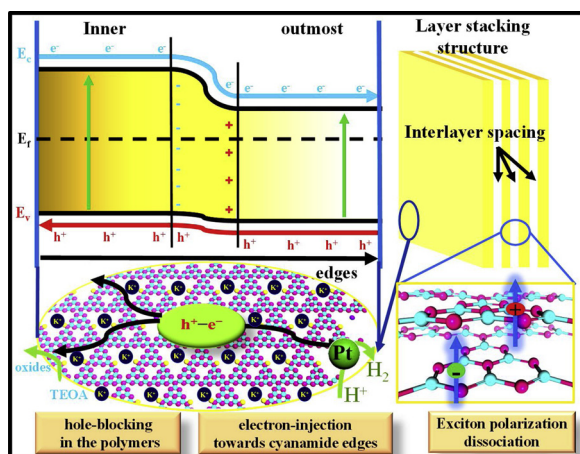
Fig. 4. (a) Steady-state PL spectra and (b) TRF kinetics of CN, crystalline CN, CCN and crystalline CCN. (c) Absolute FQY spectra of CN and crystalline CCN. (d) Mott-Schottky curves of CN and crystalline CCN.

singlet exciton lifetime indicated an enhanced single exciton dissociation in crystalline CCN [52–54]. The absolute fluorescence quantum yield (FQY) spectra was performed to evidence the contribution of crystalline and cyanamide edges to enhanced exciton dissociation (Fig. 4c). The wavelength range of exciton recombination was from 420 to 600 nm for CN and the FQY of CN was 2.40%. In contrast, the wavelength range of exciton recombination was from 490 to 617 nm for crystalline CCN and the FQY was reduced to 1.14%. Obviously, the exciton dissociation in crystalline CCN was enhanced. The lower FQY was attributed to the strong π - π interaction among molecules from the rigid conjugate planar structure of crystalline CCN. In view of the accelerated exciton dissociation, the charge carrier behavior in crystalline CCN was thereby distinct from that in CN. Fig. 4d displays the Mott-Schottky curves. The positive slopes indicated an n-type semiconductor feature. The electron concentration (N_D) in the samples can be concluded from its slope on the basis of Mott-Schottky equation:

$$\frac{1}{C^2} = \frac{2}{\varepsilon_0 A^2 e N_D} \left(V - V_{fb} - \frac{k_B T}{e} \right) \quad (5)$$

where C and A are the interfacial capacitance and area, respectively, N_D is the number of donors (electron concentration), V is the applied voltage, k_B is Boltzmann's constant, T is the absolute temperature, ε is the dielectric constant of the semiconductor, ε_0 is the permittivity of free space, V_{fb} is the flat-band potential, and e is the electronic charge. The calculated N_D in crystalline CCN was 8.56 times higher than that in CN. The improved charge transport in crystalline CCN was also reflected in its smaller electric resistance (Fig. S17a), resulting in higher photocurrent density (Fig. S17b). These results indicated that more hot electrons were produced in crystalline CCN.

The photocatalytic HERs were conducted in 10 vol% triethanolamine (TEOA) aqueous solution using 3 wt% Pt co-catalyst. The visible light photocatalytic HER rates on crystalline CN, CCN and crystalline CCN were 5.3, 8.9 and 14.9 times higher than that on CN, respectively (Fig. 5a). The HER rate on crystalline CCN reached as high as $2.69 \text{ mmol g}^{-1} \text{ h}^{-1}$. The wavelength-dependent H_2 evolution activities were further investigated. Crystalline CN and crystalline CCN had higher HER activity than CN and CCN at 450 ± 10 nm (Fig. S18a). In contrast, CCN and crystalline CCN showed much higher HER activities than CN and crystalline CN at 500 ± 10 nm (Fig. S18b), due to the stronger light absorption at this wavelength from the $n \rightarrow \pi^*$ electron transition. In all the cases, crystalline CCN exhibited the highest HER



Scheme 1. Schematic exciton dissociation and charge transfer in crystalline CCN.

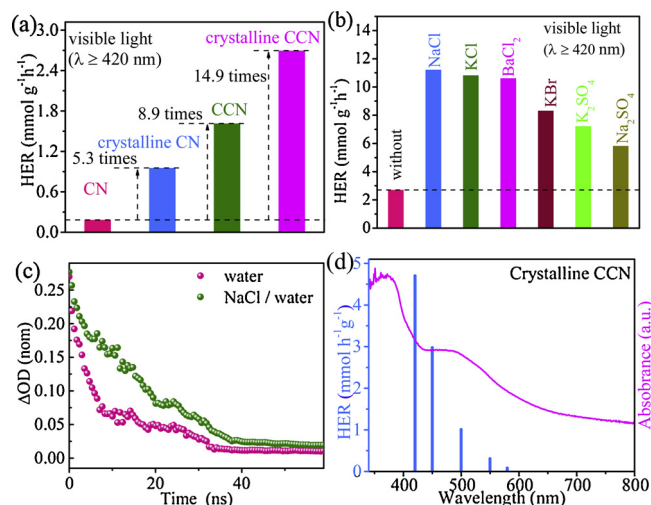


Fig. 5. Photocatalytic HERs on the photocatalysts with 3 wt% Pt in 10 vol% TEOA aqueous solution (a) in the absence or (b) in the presence of different salts under visible light ($\lambda \geq 420$ nm). (c) Intermediate timescale transient absorption kinetics monitored from 700 to 750 nm of crystalline CCN in deionized water or 3 wt% NaCl aqueous solution in the presence of 10 vol% TEOA. (d) Wavelength-dependent photocatalytic H_2 evolution activities of crystalline CCN in 3 wt% NaCl aqueous solution using 10 vol% TEOA.

activities. Besides the strong visible light absorption, the efficient exciton polarization dissociation and high electron mobility in crystalline CCN advanced the HERs. The HERs over crystalline CCN in different salt solutions (3 wt%) were studied to evaluate the effect of outside ions on the polarized surface of crystalline CCN (Fig. 5b). Interestingly, the introduction of salt ions extremely enhanced the HERs. The salt ions strengthened local electric field at the photocatalyst surface by the formation of Helmholtz layer, which promoted exciton polarization dissociation for HERs (Fig. S19). Although KBr, K_2SO_4 and Na_2SO_4 could promote the HERs, the HER activities were lower than those for NaCl, $BaCl_2$ and KCl. It should be attributed to the faster coverage rate of Cl^- with smaller volume than Br^- and SO_4^{2-} [55]. Femtosecond time-resolved transient absorption showed that the optical density (ΔOD) of crystalline CCN in NaCl aqueous solution was higher than that in deionized water (Fig. 5c). Obviously, higher optical density means higher electron density on photocatalyst surface [56], which facilitates HERs. The higher electron density may be from the oxidation of Cl^- by highly separated holes on the nonpolarized surface of crystalline CCN, and the produced Cl^\bullet/Cl would act as an electron shuttle mediator to accelerate the hole capture [50,54]. The hypothesis was verified by the experiment results that the introduction of NaCl promoted the HER for crystalline CN but had negligible effect on the HERs for CN and CCN (Fig. S20). Moreover, crystalline CCN showed a robust recyclability for HERs (Fig. S21). The AQY for HER over crystalline CCN in the presence of NaCl were 42% at 420 nm and 9% at 500 nm (Fig. 5d), which reached the art-of-the-state level for the $g-C_3N_4$ based photocatalysts reported (Table S6). In addition, the AQY for HER over crystalline CCN without Pt in deionized water was 0.89% at 420 nm and 0.08% at 500 nm (Fig. S22). The low AQY should be attributed to a two-electron process for applying carbon nitride alone for photocatalytic water splitting [57]

4. Conclusion

The texture and electronic band structures of polymeric carbon nitrides could be facilely tailored by changing KCl dosage during the polymerization of urea. The light absorption of crystalline CCN extended to 736 nm. The formation of internal electric field in crystalline CCN facilitated exciton polarization dissociation and electron transfer.

The introduction of reactive surface charges (ions) extremely enhanced the HERs, which should be attributed to the high electron density on crystalline CCN surface. This study establishes a comprehensive understanding of photocatalytic HERs using polymeric carbon nitride photocatalysts and puts forward an effective strategy for optimizing the physicochemical properties of polymeric carbon nitride photocatalysts.

Acknowledgements

This work was supported by the National Natural Science Foundation of China (51572077, 51478171, 51778218), and Hunan Provincial Innovation Foundation for Postgraduate (CX2018B164).

Appendix A. Supplementary data

Supplementary data associated with this article can be found, in the online version, at <https://doi.org/10.1016/j.apcatb.2019.03.069>.

References

- [1] X. Chen, L. Liu, Y.Y. Peter, S.S. Mao, *Science* 331 (2011) 746–750.
- [2] F.K. Kessler, Y. Zheng, D. Schwarz, C. Merschjann, W. Schnick, X. Wang, M.J. Bojdys, *Nat. Rev. Mater.* 2 (2017) 17030.
- [3] T.J. Jacobsson, V. Fjällström, M. Sahlberg, M. Edoff, T. Edvinsson, *Energy Environ. Sci.* 6 (2013) 3676–3683.
- [4] T. Le Bahers, M. Rérat, P. Sautet, *J. Phys. Chem. C* 118 (2014) 5997–6008.
- [5] T.M. Clarke, J.R. Durrant, *Chem. Rev.* 110 (2010) 6736–6767.
- [6] C. Merschjann, S. Tschierlei, T. Tyborski, K. Kailasam, S. Orthmann, D. Hollmann, T. Schedel-Niedrig, A. Thomas, S. Lochbrunner, *Adv. Mater.* 27 (2015) 7993–7999.
- [7] C. Merschjann, T. Tyborski, S. Orthmann, F. Yang, K. Schwarzburg, M. Lublow, M. Lux-Steiner, T. Schedel-Niedrig, *Phys. Rev. B* 87 (2013) 205204.
- [8] Y. Kang, Y. Yang, L.C. Yin, X. Kang, L. Wang, G. Liu, H.M. Cheng, *Adv. Mater.* 28 (2016) 6471.
- [9] Q. Liang, Z. Li, Z.H. Huang, F. Kang, Q.H. Yang, *Adv. Funct. Mater.* 25 (2015) 6885–6892.
- [10] Y. Li, R. Jin, Y. Xing, J. Li, S. Song, X. Liu, M. Li, R. Jin, *Adv. Energy Mater.* 6 (2016) 1601273.
- [11] A. Thomas, A. Fischer, F. Goettmann, M. Antonietti, J. Müller, R. Schlögl, J.M. Carlsson, *J. Mater. Chem.* 18 (2008) 4893–4908.
- [12] H. Ou, L. Lin, Y. Zheng, P. Yang, Y. Fang, X. Wang, *Adv. Mater.* 29 (2017) 1700008.
- [13] G. Zhang, G. Li, Z.A. Lan, L. Lin, A. Savateev, T. Heil, S. Zafeirotos, X. Wang, M. Antonietti, *Angew. Chem. Int. Ed.* 56 (2017) 13445–13449.
- [14] T.A. Pham, Y. Ping, G. Galli, *Nat. Mater.* 16 (2017) 401–408.
- [15] W. Hu, L. Lin, R. Zhang, C. Yang, J. Yang, *J. Am. Chem. Soc.* 139 (2017) 15429–15436.
- [16] R. Sundararaman, Y. Ping, *J. Chem. Phys.* 146 (2017) 104109.
- [17] G. Zhang, Q. Ji, Z. Wu, G. Wang, H. Liu, J. Qu, J. Li, *Adv. Funct. Mater.* 28 (2018) 1706462.
- [18] G. Liu, G. Zhao, W. Zhou, Y. Liu, H. Pang, H. Zhang, D. Hao, X. Meng, P. Li, T. Kako, *Adv. Funct. Mater.* 26 (2016) 6822–6829.
- [19] X. Fan, L. Zhang, R. Cheng, M. Wang, M. Li, Y. Zhou, J. Shi, *ACS Catal.* 5 (2015) 5008–5015.
- [20] S. Guo, Z. Deng, M. Li, B. Jiang, C. Tian, Q. Pan, H. Fu, *Angew. Chem. Int. Ed.* 55 (2016) 1830–1834.
- [21] G. Liu, P. Niu, L. Yin, H.-M. Cheng, *J. Am. Chem. Soc.* 134 (2012) 9070–9073.
- [22] Y.S. Jun, J. Park, S.U. Lee, A. Thomas, W.H. Hong, G.D. Stucky, *Angew. Chem. Int. Ed.* 125 (2013) 11083–11087.
- [23] G. Zhang, M. Zhang, X. Ye, X. Qiu, S. Lin, X. Wang, *Adv. Mater.* 26 (2014) 805–809.
- [24] J. Yuan, X. Liu, Y. Tang, Y. Zeng, L. Wang, S. Zhang, T. Cai, Y. Liu, S. Luo, Y. Pei, C. Liu, *Appl. Catal. B: Environ.* 237 (2018) 24–31.
- [25] B. Delley, *J. Chem. Phys.* 92 (1990) 508–517.
- [26] B. Delley, *J. Chem. Phys.* 113 (2000) 7756–7764.
- [27] J.P. Perdew, K. Burke, M. Ernzerhof, *Phys. Rev. Lett.* 77 (1996) 3865–3868.
- [28] G. Zhang, A. Savateev, Y. Zhao, L. Li, M. Antonietti, *J. Mater. Chem. A* 5 (2017) 12723–12728.
- [29] M. Groenewolt, M. Antonietti, *Adv. Mater.* 17 (2005) 1789.
- [30] A. Savateev, S. Pronkin, J.D. Epping, M.G. Willinger, C. Wolff, D. Neher, M. Antonietti, D. Dontsova, *ChemCatChem* 9 (2017) 167–174.
- [31] Y. Cui, Z. Ding, X. Fu, X. Wang, *Angew. Chem. Int. Ed.* 51 (2012) 11814–11818.
- [32] V. Lau, I. Moudrakovski, T. Botari, S. Weinberger, M. Mesch, V. Duppel, J. Senker, V. Blum, B. Lotsch, *Nat. Commun.* 7 (2016) 12165.
- [33] H. Yu, R. Shi, Y. Zhao, T. Bian, Y. Zhao, C. Zhou, G.I. Waterhouse, L. Wu, C. Tung, T. Zhang, *Adv. Mater.* 29 (2017) 1605148.
- [34] H. Gao, S. Yan, J. Wang, Y.A. Huang, P. Wang, Z. Li, Z. Zou, *Phys. Chem. Chem. Phys.* 15 (2013) 18077–18084.
- [35] X. Li, W. Bi, L. Zhang, S. Tao, W. Chu, Q. Zhang, Y. Luo, C. Wu, Y. Xie, *Adv. Mater.* 28 (2016) 2427–2431.
- [36] G. Zhang, Z.-A. Lan, L. Lin, S. Lin, X. Wang, *Chem. Sci.* 7 (2016) 3062–3066.
- [37] T.Y. Ma, J. Ran, S. Dai, M. Jaroniec, S.Z. Qiao, *Angew. Chem. Int. Ed.* 54 (2015) 4646–4650.

- [38] J. Xu, H. Wang, C. Zhang, X. Yang, S. Cao, J. Yu, M. Shalom, *Angew. Chem. Int. Ed.* 56 (2017) 8426–8430.
- [39] X. Fan, Z. Xing, Z. Shu, L. Zhang, L. Wang, J. Shi, *RSC Adv.* 5 (2015) 8323–8328.
- [40] H. Kim, S. Gim, T.H. Jeon, H. Kim, W. Choi, *ACS Appl. Mater. Interfaces* 9 (2017) 40360–40368.
- [41] Y. Li, J. Zhang, Q. Wang, Y. Jin, D. Huang, Q. Cui, G. Zou, *J. Phys. Chem. B* 114 (2010) 9429–9434.
- [42] A.B. orge, D.J. Martin, M.T. Dhanoa, A.S. Rahman, N. Makwana, J. Tang, A. Sella, F. Cora, S. Firth, J.A. Darr, *J. Phys. Chem. C* 117 (2013) 7178–7185.
- [43] Y. Chen, B. Wang, S. Lin, Y. Zhang, X. Wang, *J. Phys. Chem. C* 118 (2014) 29981–29989.
- [44] Y. Zhang, S. Jiang, W. Song, P. Zhou, H. Ji, W. Ma, W. Hao, C. Chen, J. Zhao, *Energy Environ. Sci.* 8 (2015) 1231–1236.
- [45] S. Trasatti, *Pure Appl. Chem.* 58 (1986) 18077.
- [46] X. He, G. Zhu, J. Yang, H. Chang, Q. Meng, H. Zhao, X. Zhou, S. Yue, Z. Wang, J. Shi, L. Gu, D. Yan, Y. Weng, *Sci. Rep.* 5 (2015) 17076.
- [47] G. Dong, K. Zhao, L. Zhang, *Chem. Commun.* 48 (2012) 6178–6180.
- [48] S. Pekar, *Zh. Eksperim. i Teor. Fiz.* 16 (1946) 933.
- [49] J. Zhang, G. Zhang, X. Chen, S. Lin, L. Möhlmann, G. Dołęga, G. Lipner, Antonietti, S. Blechert, X. Wang, *Angew. Chem. Int. Ed.* 124 (2012) 3183–3187.
- [50] Z. Zeng, X. Quan, H. Yu, S. Chen, Y. Zhang, H. Zhao, S. Zhang, *Appl. Catal. B: Environ.* 236 (2018) 99–106.
- [51] Y. Zhao, Y. Zhao, G.I.N. Waterhouse, L. Zheng, X. Cao, F. Teng, L.Z. Wu, C.H. Tung, D. O'Hare, T. Zhang, *Adv. Mater.* 29 (2017) 1703828.
- [52] M. Yang, Y. Xu, W. Lu, K. Zeng, H. Zhu, Q. Xu, G.W. Ho, *Nat. Commun.* 8 (2017) 14224.
- [53] H. Wang, X. Sun, D. Li, X. Zhang, S. Chen, W. Shao, Y. Tian, Y. Xie, *J. Am. Chem. Soc.* 139 (2017) 2468–2473.
- [54] H. Wang, S. Jiang, S. Chen, X. Zhang, W. Shao, X. Sun, Z. Zhao, Q. Zhang, Y. Luo, Y. Xie, *Chem. Sci.* 8 (2017) 4087–4092.
- [55] Z. Chen, Q. Zhang, Y. Luo, *Angew. Chem. Int. Ed.* 57 (2018) 5320–5324.
- [56] K.L. Corp, C.W. Schlenker, *J. Am. Chem. Soc.* 139 (2017) 7904–7912.
- [57] J. Liu, Y. Liu, N. Liu, Y. Han, X. Zhang, H. Huang, Y. Lifshitz, S.T. Lee, J. Zhong, Z. Kang, *Science* 347 (2015) 970–974.